PNAS RESEARCH ARTICLE | ENGINEERING

Atomistic measurement and modeling of intrinsic fracture toughness of two-dimensional materials

Xu Zhang[a,1], Hoang Nguyen[a,1], Xiang Zhang[b], Pulickel M. Ajayan[b], Jianguo Wen[c,2], and Horacio D. Espinosa[a,d,2]

Edited by Risto Nieminen, Aalto-yliopisto Teknillisen fysiikan laitos, Aalto, Finland; received April 18, 2022; accepted September 14, 2022

Quantifying the intrinsic mechanical properties of two-dimensional (2D) materials is essential to predict the long-term reliability of materials and systems in emerging applications ranging from energy to health to next-generation sensors and electronics. Currently, measurements of fracture toughness and identification of associated atomistic mechanisms remain challenging. Herein, we report an integrated experimental–computational framework in which in-situ high-resolution transmission electron microscopy (HRTEM) measurements of the intrinsic fracture energy of monolayer MoS_2 and $MoSe_2$ are in good agreement with atomistic model predictions based on an accurately parameterized interatomic potential. Changes in crystalline structures at the crack tip and crack edges, as observed in in-situ HRTEM crack extension tests, are properly predicted. Such a good agreement is the result of including large deformation pathways and phase transitions in the parameterization of the inter-atomic potential. The established framework emerges as a robust approach to determine the predictive capabilities of molecular dynamics models employed in the screening of 2D materials, in the spirit of the materials genome initiative. Moreover, it enables device-level predictions with superior accuracy (e.g., fatigue lifetime predictions of electro- and opto-electronic nanodevices).

atomistic measurements | fracture energy | transition metal dichalcogenide | atomistic J integral | bond dissociation

The past decade has seen unprecedented progress in the growth, chemical functionalization, transfer, and assembly of two-dimensional (2D) materials–based systems (1), with applications ranging from energy (2) to optics (3), electronics (4), biodetection (5), and structural materials (6). They represent exciting developments of this decade, addressing societal needs in energy, materials, and high-performance electronics. In all these applications, the mechanical reliability of 2D materials is a practical engineering concern. Therefore, quantifying accurately how and when 2D materials fail has become an essential part of understanding device reliability to prevent catastrophic events that can compromise their functionality. Attaining such accuracy has been a major challenge, yet without it, excessive errors in the estimation of the service lifetime of 2D material–based devices would inevitably arise.

The unique monolayer structure of 2D materials enables direct observation of the propagation of atomically sharp cracks (7, 8), making the aforementioned objective achievable. Such observations can also facilitate a fundamental understanding of failure mechanisms and enable comparison between experimental and theoretical calculations (e.g., fracture energy via Griffith and J-integral). In turn, the comparison has the potential to impact the assessment of functionality and robustness of micro- and nanodevices in various applications.

Prior experimental approaches were mainly based on in-situ scanning electron microscopy and transmission electron microscopy (TEM) techniques (9–13). For example, in-situ scanning electron microscopy fracture tests were conducted for monolayer graphene (14) and hexagonal Boron Nitride (h-BN) (15). In both these studies, the measured fracture toughness significantly exceeded the Griffith's criterion prediction, i.e., two times the surface energy estimated from ab initio simulations. This appears contradictory to the brittle nature of graphene and h-BN in their pristine form. Hence, researchers attributed the higher fracture toughness to the existence of grain boundaries, in the case of graphene, and to structure-induced crack deflection and branching in the case of h-BN, both inferred solely from computer simulations due to the inability of scanning electron microscopy to provide images with atomic-resolution. In the abscense of atomistic observations, none of these inferences can be confirmed or rejected. In an attempt to overcome such limitation, in-situ scanning transmission electron microscopy (STEM) experiments were performed on monolayer and bilayer ReS_2, and toughness estimated based on linear elastic fracture mechanics

Significance

The promise of computational material design is based on atomistic models with predictive capabilities. While quantum chemistry simulations can be used during unit cell property screening of two-dimensional (2D) materials, device-level analysis requires large-scale atomistic simulations employing interatomic potentials. We present advances in experimentation and machine learning–inspired algorithms for accurate interatomic potential selection, parameterization, and validation. Through in-situ high-resolution transmission electron microscopy atomistic measurements, we directly compare atomic structures and material fracture toughness with those predicted by molecular dynamics simulations employing a potential informed by ab initio data in the nonequilibrium regime. The integrated framework provides a robust approach to obtaining intrinsic mechanical properties of 2D materials (in their pristine and defective states) and informs the analysis of device reliability with unprecedented accuracy.

The authors declare no competing interest.

This article is a PNAS Direct Submission.

[1]Xu Zhang and H.N. contributed equally to this work.

[2]To whom correspondence may be addressed. Email: jwen@anl.gov or espinosa@northwestern.edu.

This article contains supporting information online at http://www.pnas.org/lookup/suppl/doi:10.1073/pnas.2206756119/-/DCSupplemental.

Published November 4, 2022.

(LEFM) (7). All these studies exemplify the challenges encountered while conducting in-situ fracture experiments on 2D materials from sample preparation to atomistic quantifications, which involve 1) the transfer of 2D flakes from the growth substrate (or the solution phase) onto a microelectromechanical system, 2) the definition of a regular sample geometry using focused ion beam (FIB) milling, and 3) the creation of a crack with either electron beam irradiation or FIB milling. We note that the yield of experimental measurements, after all these steps, is currently very low. Consequently, establishing experiments and protocols that can reveal intrinsic fracture properties of 2D materials is highly needed to evaluate their functionality and durability in diverse application environments. To date, such measurements are in their infancy.

Molecular Dynamics (MD) simulations based on interatomic potentials have also been employed to study the fracture of 2D materials (6) but with limited success. The first challenge arises while selecting/parameterizing interatomic potentials that are accurate in the large deformation regime (where bond dissociation and breaking occurs). We found that interatomic potentials parameterized primarily for equilibrium properties often show poor transferability at large deformations (16). The second challenge is whether to trust atomic reconstructions/phase transitions observed in in-silico fracture simulations, which are yet to be identified in experiments. While ab initio simulations based on density functional theory (DFT) can confirm the ground-state stability of 2D material structures, such validations are limited in size and finite temperature effects. To overcome this limitation, we recently developed an interatomic potential parameterization approach that incorporated data from relevant DFT calculations, an optimizer using a multiobjective genetic algorithm, and statistical analyses that can be used to improve the predictive power over successive iterations. These elements allowed for selection/parameterization of interatomic potentials that capture atomic changes in the large deformation regime while preserving near-equilibrium accuracy (16). However, such a parameterization framework still requires experimental validations in the context of fracture, which demands direct in-situ atomic characterizations.

Herein, we report in-situ high-resolution transmission electron microscopy (HRTEM) fracture tests and MD fracture simulations, based on an independently parameterized Tersoff potential, on two representative 2H-transition metal dichalcogenide materials (2H-TMDs). The results reveal that the intrinsic fracture toughness of monolayer MoS_2 and $MoSe_2$ approaches the values predicted by both ab initio and MD simulations. In addition, we show that the parameterized interatomic potential, used in the MD simulations, is able to capture experimentally observed atomic reconstructions in the vicinity of the crack tip and edges. Moreover, there is good agreement in the critical energy release rate (i.e., the J integral) (17, 18) computed from both experimental and computational atomic data (strain–stress fields in the near-tip). The high accuracy achieved herein enables ∼150 times less error in the fatigue life prediction of nanodevices fabricated from pristine 2D materials, in comparison with existing measurement via in-situ scanning electron microscopy techniques. It is worth noting that the analyses here reported are unattainable without an integrated experimental–numerical framework, which makes possible the unambiguous quantification of 2D materials' fracture energy. Such a framework is extremely useful in assessing the predictive capability of atomistic models used in materials design, especially those based on artificial intelligence.

In Situ HRTEM Fracture Tests

Fracture tests were conducted with in-situ HRTEM (FEI Titan 80-300 TEM with an image corrector for both chromatic and spherical aberrations) using electron beam irradiation for the initiation and stable propagation of cracks. Such a setup differs from conventional fracture tests in two respects: 1) strain fields, in the vicinity of the crack tip, are directly computed from images of atomic positions, and 2) stress fields are obtained from a nonlinear constitutive law identified from DFT. Monolayer MoS_2 and $MoSe_2$ flakes (Fig. 1 *A* and *B*), synthesized by chemical vapor deposition, were transferred to holey Si_3N_4 TEM grids to form suspended membranes. After monolayer transfer, the sample preparation included a thermal treatment for 2h at 130 °C in a 1×10^{-7} Torr vacuum to remove potential contamination. We note that a previous study conducted by our group showed that for the TMDs used in this study, the current procedure adequately provides a clean and well-preserved sample structure. In particular, Dong et al. (19) showed that the same annealing process successfully removed contaminants as inferred from HRTEM and Raman characterization (see *SI Appendix*, *SI Materials and Methods*; *SI Appendix*, Fig. S1). In addition, images with similar quality level, contrast and atom definition, were reported in (7, 8, 20, 21).

To generate a dominating crack, the suspended monolayer flakes were irradiated by a focused electron beam under 200-kV acceleration voltage for ∼1 to 2 min. The electron beam was tuned into a narrow slit (width of <5 nm) along the zigzag direction of the suspended monolayer (Fig. 1*C*) and successfully used to knock out atoms leading to an atomically sharp crack. Fracture experiments were then performed at room temperature (296 K). For the sole purpose of explaining the process of crack loading and growth during TEM experimentation, we consider a simplified model consisting of a crack with length $2a$ in a circular membrane (2D specimen) with radius R (Fig. 2*A*). The membrane is subjected to a prescribed radial strain arising from the transfer process and adhesion between the membrane and the holey substrate. An FEA (finite element analysis) estimate of the energy release rate for such geometry is

$$\mathcal{G} = \frac{E\delta^2}{R(1-\nu)}\sqrt{\pi\alpha}\; p(\alpha), \qquad [1]$$

where $\alpha = a/R$, δ/R is the radial strain of the circular membrane computed from the radial displacement δ, E is the Young's modulus, and ν is the Poisson ratio of the material ($MoSe_2$ or MoS_2). Moreover,

$$p(\alpha) = (1-\alpha)\left[0.33 + \alpha\left(1.50 - 2.45\alpha + 2\alpha^2\right)\left(5.72 - 2.3(1-\alpha) + 2.24(1-\alpha)^2\right)\right]. \qquad [2]$$

The examination of applied $\mathcal{G}$ as a function of crack length (Fig. 2*B*) reveals that a crack would start to grow when the energy release rate is equal to the material's fracture resistance (i.e., $\mathcal{G} = R$) and when the crack resistance, R, grows at a smaller rate than $\mathcal{G}$ with respect to the crack length extension, i.e., $\partial\mathcal{G}/\partial a \geq \partial R/\partial a$ (point 1 in Fig. 2*B*). Under this condition, crack growth would occur spontaneously, and any excess in driving energy would be converted into kinetic energy. When $\partial\mathcal{G}/\partial a < \partial R/\partial a$ (point 2 in Fig. 2*B*), the crack will stop growing. At this point, the growth of the crack reduces the stiffness of the membrane, and hence reduces the crack-driving force.

In a perfectly brittle material, $R = G_f$, and $\partial R/\partial a = 0$. However, a minute amount of polymer residue, which could be outside of the high-resolution imaging area, would cause a small but finite $\partial R/\partial a$ and a certain level of viscosity. Such a

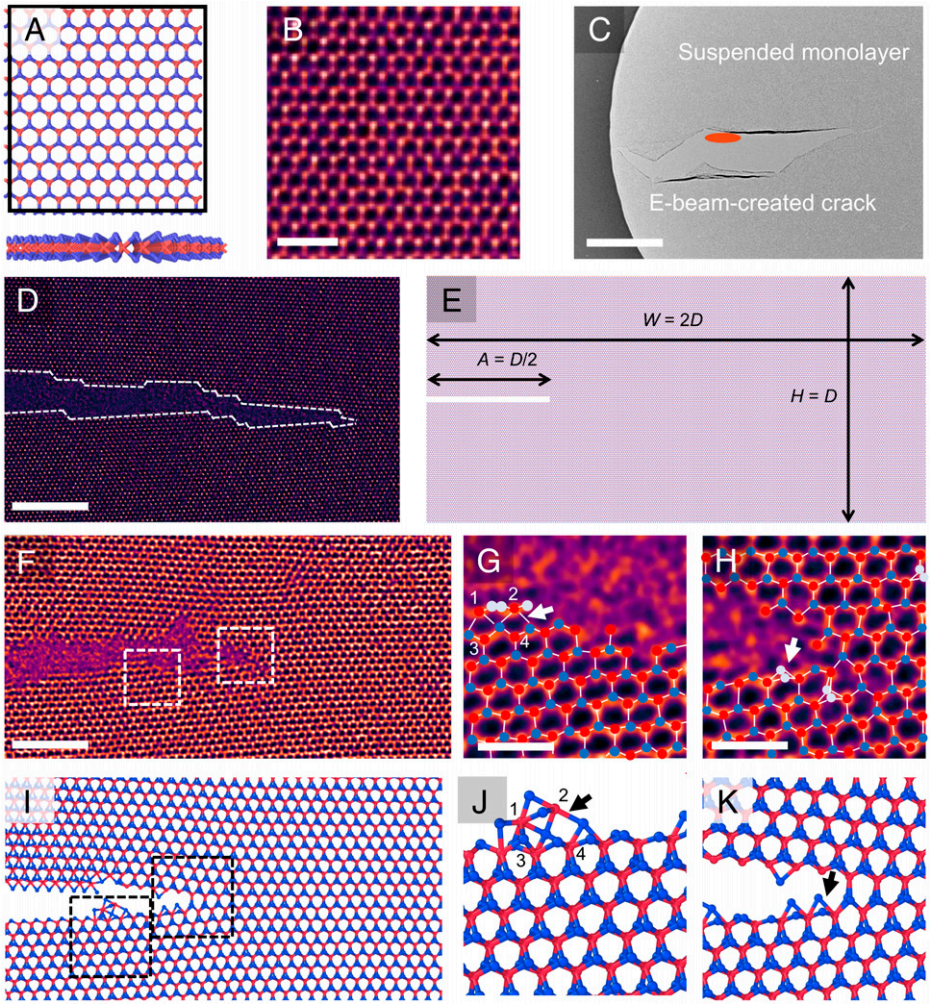

Fig. 1. Lattice structures, crack initiation, and atomic configurations at the crack tip. (*A*) Atomic structures of monolayer MoS_2 and $MoSe_2$. Red atoms are Mo, and blue atoms are S (in MoS_2) or Se (in $MoSe_2$). (*B*) HRTEM images of as-synthesized monolayer $MoSe_2$. (Scale bar: 1 nm.) (*C*) A crack created in a suspended monolayer $MoSe_2$ flake by electron beam irradiation. The electron beam was tuned into a slit along the zigzag direction of the suspended monolayer, as indicated by the orange ellipse. (Scale bar: 0.4 μm.) (*D*) Crack path in monolayer $MoSe_2$ under continuous electron beam irradiation. The crack followed a serrated path along the zigzag direction of the monolayer $MoSe_2$ specimen. (Scale bar: 5 nm.) (*E*) The configuration used in MD simulations of fracture in monolayer MoS_2 and $MoSe_2$. $D = 40$ nm. (*F*) HRTEM image of the crack tip in monolayer $MoSe_2$. (Scale bar: 3 nm.) (*G*) Zoomed-in view of the left dashed rectangular region in *F*. Mo atoms are colored red, Se atoms are colored white, and Se_2 columns are colored blue. The arrow points at a reconstruction site, in which the four numbered Mo atoms arrange into a rectangular lattice surrounding the center Se_2 column. (Scale bar: 1 nm.) (*H*) Zoomed-in view of the right dashed rectangular region in *F*. The color coding is identical to that in *G*. The arrow points at a perturbed Se_2 site, in which the top and bottom Se atoms, with respect to the middle Mo atoms, are both visible. (Scale bar: 1 nm.) (*I*) MD snapshot of the crack tip in monolayer $MoSe_2$. (*J*) Zoomed-in view of the left dashed rectangular region in *I*. The same lattice reconstruction reported in *G* is observed and highlighted. (*K*) Zoomed-in view of the right dashed rectangular region in *I*. The same perturbed Se site discussed in *H* is observed and highlighted. The color coding in *I*–*K* is identical to that in *A*.

condition would decelerate the crack extension when $\mathcal{G}$ reaches G_f This could also explain that, when the crack length reached point 1 (at a dose rate of $\sim 2.5 \times 10^7$ $e^- \cdot nm^{-2} \cdot s^{-1}$), it started to propagate at an average velocity of ~ 2.5 $nm \cdot s^{-1}$. This allowed us to track the crack tip continuously and hence enabled the acquisition of high-resolution images, which were then used to quantify the fracture toughness following the procedure described in *Fracture Toughness Quantification* (J-integral calculation). We note that a similar electron beam–induced crack propagation was also observed in a previous HRTEM investigation of monolayer MoS_2 (8). Furthermore, electron irradiation studies reported the formation of vacancies (19, 22) and larger defects, such as vacancy clusters (23) and vacancy lines (22, 24), upon prolonged electron beam irradiation of transition metal dichalcogenides. In the fracture tests conducted herein, we controlled the imaging electron dose such that vacancy defects were reduced to a minimum and the impact on the quantified toughness was very small (see below for a discussion of vacancies quantification and their effect on toughness).

A typical crack path, in monolayer $MoSe_2$, during the stable crack propagation stage is shown in Fig. 1*D*. The HRTEM image was taken at an acquisition rate of 10 Hz and a defocus value between −10 and −5 nm, under which the crack remained stationary. The crack followed a serrated path along the zigzag direction of the suspended $MoSe_2$ monolayer due to its lower surface energy in comparison with the armchair direction (16). We also acquired HRTEM images at a defocus value of −5 to 0 nm, under which the Mo and S/Se atoms became visible (Fig. 1*F*). Such imaging allows for direct comparison of the atomic configuration at the crack tip between experiments and MD simulations, as discussed next.

MD Simulations of Fracture

The MD fracture simulations for monolayer MoS_2 and $MoSe_2$ (at 296 K) were conducted employing the Tersoff potential (25), which was shown to possess good accuracy and transferability for thermal and mechanical properties of monolayer

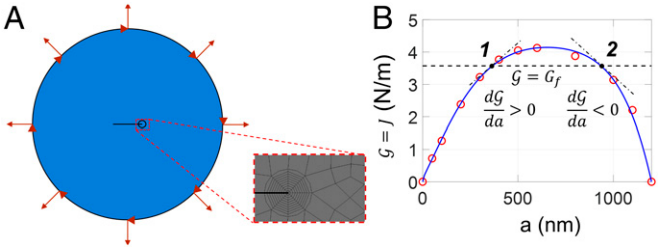

Fig. 2. (*A*) Loading configuration for a membrane suspended over a holey substrate subjected to a fixed displacement caused by the adhesion between $MoSe_2$ and Si_3N_4 (the inset figure shows the detail of the mesh at the crack tip). (*B*) Plot of the energy release rate as a function of crack size and snap-through instability during crack extension (red circles indicate the data from finite element calculations, and the solid blue line is an approximated curve based on Eq. **1**).

$MoSe_2$ (16). Herein, we utilize the parameterization framework, detailed in our earlier work (16), to augment the parameterization of the Tersoff potential to describe fracture of monolayer MoS_2 and $MoSe_2$. The parametrization process contains three steps: training, screening, and evaluation. The training step includes the application of a multiobjective genetic algorithm for the optimization of key far-from-equilibrium material properties (e.g., dissociation energy landscapes and dissociation forces against ab initio calculations). The optimized interatomic potential parameter sets were then screened for accuracy by employing another set of properties. Finally, the screened parameter sets were evaluated for properties beyond the training and screening datasets to ensure sufficient transferability. In this study, we exploited the versatility of the parameterization approach and the correlation matrix statistical analyses to further capture a bond dissociation behavior as encountered in the fracture process. As shown in *SI Appendix*, Fig. S2, the Mo–Se bonds above and below the Mo atom break sequentially when the crack propagates along the zigzag direction, resulting in a more gradual energy release process and an intermediate state during the uniaxial elongation along the armchair direction. To capture such a state, we added corresponding stress–strain curves as training data (*SI Appendix*, Fig. S2). We further included force fitting for the dissociation energy landscapes of Se and S clusters. Moreover, in the screening step, we prioritized parameter sets that can accurately capture such intermediate states. The enrichment allowed the Tersoff potential to capture lattice distortions observed experimentally near the crack tip in monolayer $MoSe_2$, as discussed in subsequent sections.

To simulate fracture in the suspended MoS_2 and $MoSe_2$ monolayers, an 80 by 40 nm rectangular domain containing a 20 nm long pre-crack (obtained by removing 5 atomic layers) was loaded along the armchair direction (y direction in Fig. 1*E*). The boundary conditions were free at the left and right edges of the specimen and periodic at the top and bottom. In the experiment, the monolayers were not completely free in the out-of-plane direction but restrained by adhesion with the TEM grids. Hence, to mimic the experimental condition we added potential surfaces, at a distance of 20 Å away from the monolayer, to prevent large out-of-plane motions. The loading was applied at a strain rate of 10^8 s^{-1} until the onset of crack propagation was detected. A second run was conducted from the state right before crack propagation, under a strain rate of 5 x10^6 s^{-1} (see Supporting Information, Materials and Methods).

Fracture Toughness Quantification

To quantify the fracture toughness in the nonlinear regime, we utilized the J integral (18, 26), a path-independent integral that results in the strain energy release rate of the material. For brittle materials, the integral equals the fracture toughness evaluated from LEFM. Fig. 3*A* shows the atomic configuration captured in an $MoSe_2$ monolayer prior to crack propagation with the tip extending by 5 nm in 2 s (Fig. 3*B*). Similarly, Fig. 3*C* displays the onset of crack extension in the MD fracture simulation. The calculation of the J-integral followed slightly different protocols for the HRTEM in-situ experiments and MD simulations, which are detailed in *SI Appendix*, *SI Materials and Methods*. Briefly, we extracted the atomic strains (Green–Lagrangian strains E_{xx}, E_{yy}, and E_{xy}) from the HRTEM images using the structural template matching method reported in Madsen et al. (27) and computed the corresponding Cauchy stress (σ_{xx}, σ_{yy}, and σ_{xy}) using elastic constants (up to the third order) obtained from first-principle DFT calculations. The extrapolated pixel-wise E_{yy}, E_{xy}, σ_{yy}, and σ_{xy} values for the image depicted in Fig. 3*A*, are shown in Fig. 3 *D*, *E*, *G*, and *H*, respectively. For the MD simulations, we first mapped the displacement field from atomic positions (Fig. 3*F*) using a cylindrical kernel function (with an averaging radius of 3 Å) and calculated the strain field based on a numerical gradient approximation (28). The stress field is mapped independently based on the per-atom virial stress output (29) (Fig. 3 *I* and *K*). We note that this stress only carries an approximated meaning in the case of many-body interatomic potentials, like Tersoff. This stems from the equal distribution of many-body terms among the contributing atoms, leading to a nonconserving field. To achieve a more accurate mapping, central constraints must be applied (30). However, we employ the approximation in the view that it was shown to achieve a continuum stress within 5% of the exact value (31).

The stress fields σ_{xy} and σ_{yy} , obtained from MD simulations and fracture experiments at the onset of crack propagation, are reported in Fig. 3 *I*, *K* (MD simulations), *G*, and *H* (HRTEM experiments). Good agreement of the stress fields is observed, which confirms the presence of mode I loading in the suspended sample in the fracture experiments. The plotted fields display stress concentration and relaxation ahead and behind the crack tip with some minor oscillations, with the oscillatory field more pronounced in the experimental fields. Several factors are found to introduce noise in the experimental strain measurement, including thermal vibration of atoms, electron beam defocusing, unwanted sample tilt, and instrumental noise (27). The thermal vibration and instrumental noises can be reduced by image overlay and image filtering (three to four images were overlaid and processed by a Wiener filter prior to strain measurement), whereas noise introduced by defocus and unwanted sample tilt was not directly removed/minimized and thus, should be the dominant components. Plotting σ_{yy} along the *x* direction as a function of distance from the crack tip (Fig. 3*J*) reveals that the stress follows LEFM, except for a very small region at the crack tip where nonlinearities limit the stress. The comparison also suggests that this length can be considered a characteristic dimension for the fracture process zone. The existence of this nonlinear zone supports the use of the J-integral to quantify a more accurate fracture energy compared with the K-field solution. This plot also reveals a far-field stress of ~7.5 GPa at the onset of crack propagation.

The critical energy release rates J_c, calculated from HRTEM images (averaged over three cases) and MD simulations (averaged over six cases), are 3.57 ± 0.23 and 3.18 ± 0.27 $N{\cdot}m^{-1}$, respectively (*SI Appendix*, Table S3 shows all of the data). Such values are very close to the fracture toughness of monolayer $MoSe_2$ computed as $2\gamma_{MoSe2}$ = 3.1 $N{\cdot}m^{-1}$ (Griffith's criterion),

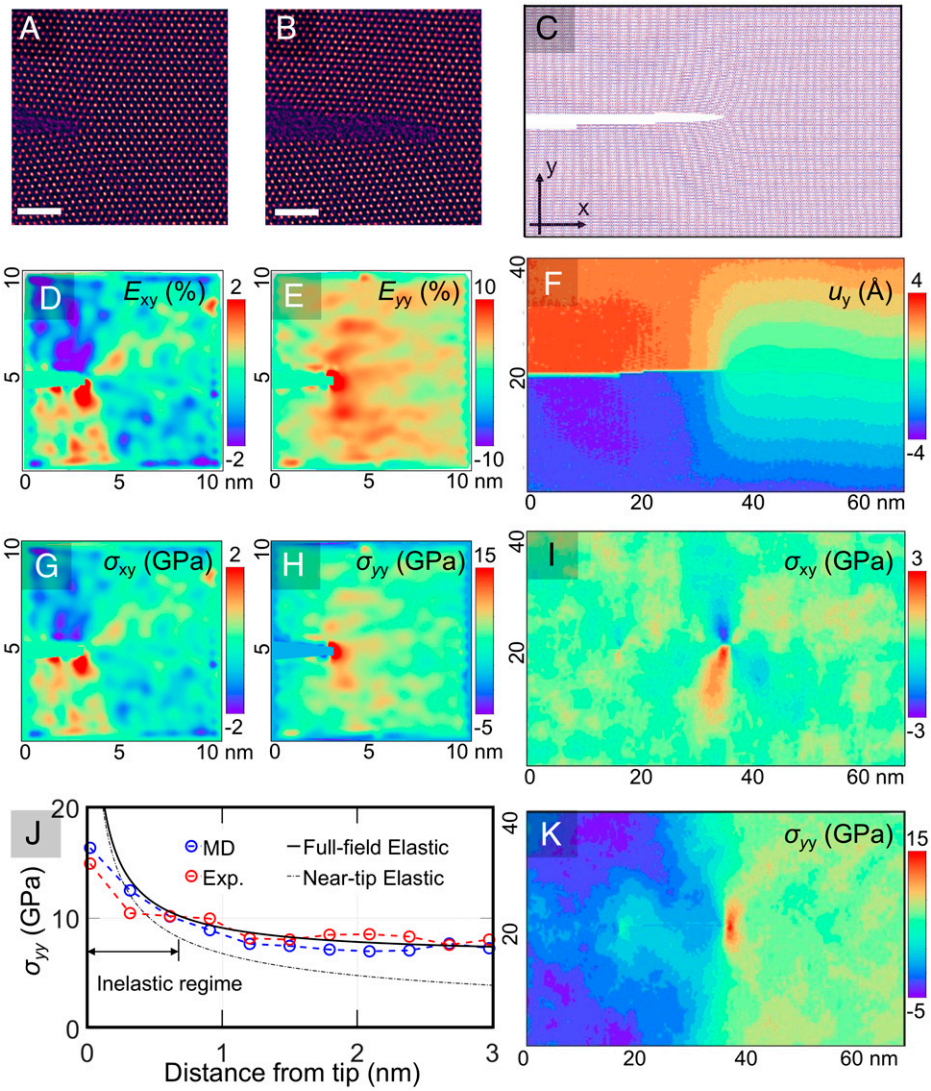

Fig. 3. Atomic strain and stress fields near the crack tip. (*A* and *B*) Crack tip configuration at the onset (*A*) and after (*B*) crack propagation. (Scale bars: 2 nm.) (*C*) Onset of crack propagation in MD fracture simulations. (*D* and *E*) Green–Lagrangian strain fields E_{xy} (*D*) and E_{yy} (*E*) for the atomic configuration shown in *A*. (*F*) Displacement field u_y for the atomic configuration shown in *C*. (*G* and *H*) Cauchy stress σ_{xy} and σ_{yy} for the atomic configuration shown in *A*. (*I*) Cauchy stress σ_{xy} for the atomic configuration shown in *C*. (*J*) Cauchy stress σ_{yy} in front of the crack tip, $MoSe_2$, for MD and experiments. Comparison with predictions from the K_I field (near-tip asymptotic elastic solution) and full-field elastic solutions. The inelastic regime corresponds to a fracture process zone of ∼1 nm. (*K*) Cauchy stress σ_{yy} for the atomic configuration shown in *C*.

where γ is the zigzag surface energy of $MoSe_2$ obtained from DFT. The computationally identified process zone with a characteristic dimension of ∼1 nm agrees well with the experimental counterpart. Similarly, for monolayer MoS_2, the fracture toughness values from HRTEM images and MD simulations are 3.92 ± 0.07, and 3.37 ± 0.23 $N{\cdot}m^{-1}$, respectively (*SI Appendix*, Table S3 shows all of the data). The Griffith's criterion results in $2\gamma_{MoS2} = 3.43$ $N{\cdot}m^{-1}$. We note that such an accuracy in the reported values of fracture toughness for monolayer MoS_2 and $MoSe_2$,using three sources of measurments (MD, DFT, and HRTEM), has not been reported elsewhere. This consistency was achieved by 1) an accurate atomic strain quantification in the as-synthesized materials, enabled by HRTEM characterizations, and 2) well-parameterized interatomic potentials possessing good accuracy in both equilibrium and large-deformation regimes. The results confirm that monolayer MoS_2 and $MoSe_2$ are intrinsically brittle materials.

In in-situ HRTEM experiments, vacancies are inevitably created during imaging even at a small dose of electron irradiation. Therefore, we conducted additional experiments to characterize the types of vacancies that can appear on $MoSe_2$ monolayers and their densities when the monolayers were exposed to the electron dose rate used in the observation step. *SI Appendix*, Fig. S6 shows that under this dose rate, the density of the most common type of vacancy (isolated selenium vacancy) does not significantly alter the fracture response of $MoSe_2$. The same conclusion can be drawn for MoS_2.

Atomic Configuration at the Crack Tip

Fig. 1 *F* and *I* shows the atomic configuration of monolayer $MoSe_2$ at the crack tip as observed in the HRTEM fracture tests and MD simulations, respectively. In Fig. 1*F*, Mo atoms are not readily distinguishable from S/Se atoms given their similar contrast. Following the protocol developed by Wang et al. (8), we determined Se atoms according to the higher density of Se and Se_2 vacancies in comparison with Mo vacancies in the monolayer $MoSe_2$ flake. Consistent with experimental observation, the crack in the MD simulations followed the zigzag direction and underwent mild deflection (Fig. 1*I*). Some unique atomic

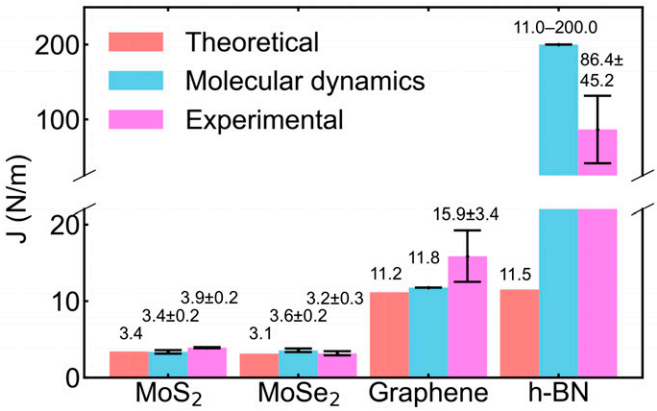

Fig. 4. Fracture toughness measurements of various 2D materials. Data for MoS_2 and $MoSe_2$ are from this study. Data for graphene are from Zhang et al. (36). Data for h-BN are from Yang et al. (15). In Yang et al. (15), a range of fracture toughness for monolayer h-BN was predicted from MD simulations; the maximum value is plotted.

configurations were identified in both the HRTEM image and MD snapshot. In Fig. 1 *G* and *J*, the four Mo atoms at the crack edge rearranged into a rectangular shape, and the Se atoms at the center of the rectangle had a coordination number of four instead of three. Such a configuration resembles the inversion domain formed in monolayer $MoSe_2$ as a result of thermal annealing and electron beam irradiation (32). It further indicates that the lattice rearrangements depend only on local atomic environments and bond breakage and are not affected by what causes bond breakage. In Fig. 1 *H* and *K*, Se atoms above and below the middle Mo layer were both visible. For MD simulations, this is the outcome of enrichment of the training data, which provides an intermediate energy state during bond dissociation (*SI Appendix*, Fig. S2). The qualitative agreements between HRTEM images and MD snapshots suggest good accuracy by the parameterized Tersoff potential and its ability to capture various atomic environments.

Discussion

Fig. 4 is a plot of the fracture toughness of monolayer MoS_2 and $MoSe_2$ measured herein as well as existing results for monolayer graphene (14) and h-BN (15). The experimental measurements for monolayer graphene and h-BN, based on an in-situ scanning electron microscopy setup, are both higher than their corresponding theoretical values for pristine materials. While such enhancements were explained via hypotheses and MD simulations, the resolution of scanning electron microscopy limits examination of other possibilities that may also increase the fracture toughness. For instance, a blunt crack tip that has a radius of a few nanometers, can reduce the stress concentration (33) and lead to an apparent higher fracture toughness if such an effect is not accounted for in the calculation of toughness. Polymer residues from the transfer process, even atomically thin, may enhance the fracture toughness of 2D materials through an extrinsic crack-bridging mechanism (34, 35). HRTEM imaging, as in this report, allows us to verify the existence of an uncontaminated crystalline phase at the crack tip region. It also provides not only accurate measurement of intrinsic fracture properties but also, quantitative validation of parameterized interatomic potentials, a feature very important in assessing force fields employed in the computational design of new materials.

We envision that the integrated experimental–computational framework here presented will be applicable to most 2D materials beyond the TMDs family. As illustrated in Fig. 5, the experimental setup requires transfer of 2D materials over holey TEM grids, which can be achieved through solution-based methods (37), dry transfer techniques (38, 39), and polymer-assisted wet transfer methods (23, 40, 41) depending on how the 2D materials are synthesized. The parameterization framework was shown to be versatile and applicable to many interatomic potentials (e.g., Buckingham, Stillinger–Weber, and Tersoff potentials and the reactive empirical bond order potential for TMDs, or REBO-TMDs) (16). As such, it covers various options for a variety of 2D materials and opens the opportunity to select the more

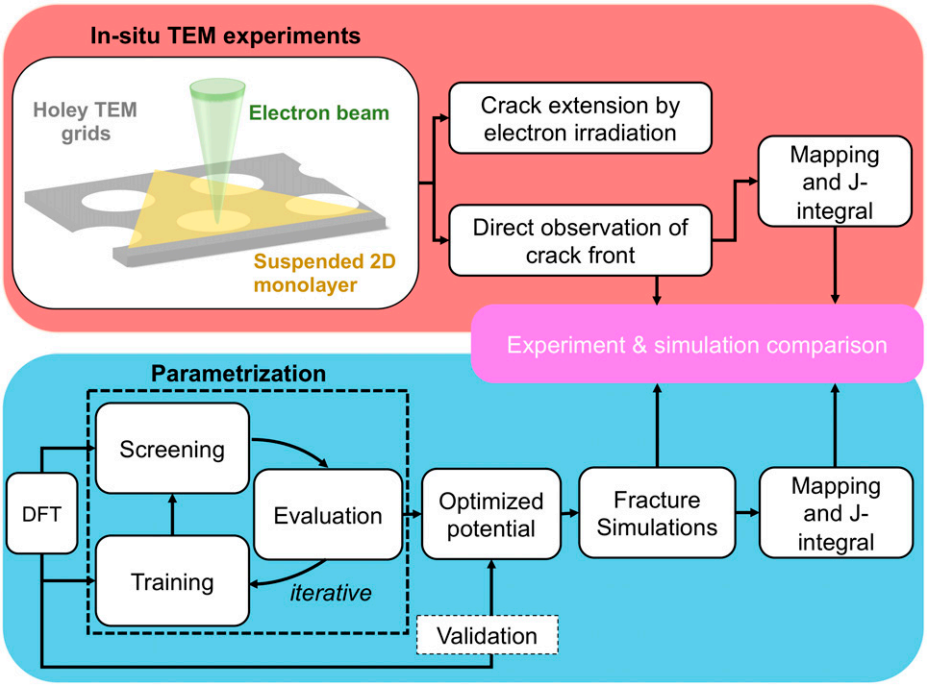

Fig. 5. Integrated experimental–computational framework to explore the intrinsic fracture properties of 2D materials.

accurate potential for a specific application. Lastly, by combining experimental and computational methodologies, we demonstrated a way to validate parameterized interatomic potential via examination of the atomic configurations at the crack tip and quantification of the fracture toughness.

To emphasize the importance of improving the accuracy of toughness measurement and quantification, we discuss its use in the assessment of reliability of nanodevices. It was shown that in graphene, the extension of cracks through a fatigue mechanism could occur at a stress level much lower than the critical stress that triggered an unstable crack propagation (42). This has important implications in practical application [e.g., a nanodevice consisting of a 2D material monolayer suspended over a gap (43) and subjected to fluctuations in applied voltage or vibrations; a common example of such a device is a mechanical nanoresonator (44, 45)]. In the case of electrical actuation (46), Joule heating from a back-gate voltage can cause an oscillating temperature of ΔT. Such oscillation imposes a cyclic eigenstrain on the suspended monolayer, which results in an oscillating stress $\Delta\sigma$ (47, 48). At the same time, there is typically a prestress within the monolayer σ_{ave} (47) caused by its adhesion with the substrate and averaged operating temperature.

As a result of this cyclic load, an initial vacancy of length a_0 can extend and reach a critical length a_c, at which the crack propagates dynamically, leading to the failure of such a nanodevice. The extension rate of the crack and the change in the stress intensity factor of the structure are related by

$$\frac{da}{dN} = C\left(\frac{\Delta K_I}{K_{Ic}}\right)^n, \qquad [3]$$

where N is the number of cycles, C and n are constants, and the change in stress intensity factor is related to the geometry of the device and change in stress via $\Delta K_I = \beta\Delta\sigma\sqrt{\pi a}$. From fracture mechanics, $a_c = K_{Ic}^2/\beta\sigma_{ave}$. Integrating **3** with respect to a yields

$$N_c = \frac{2K_{Ic}^n}{C\beta^n\Delta\sigma^n\pi^{n/2}(n-2)}\left[\frac{1}{a_0^{n/2-1}} - \left(\frac{K_{Ic}}{\beta\sqrt{\pi}\sigma_{ave}}\right)^{2-n}\right], \qquad [4]$$

which is often referred to as fatigue lifetime. We estimate the values of $C = 0.0032$ nm/cycle and $n = 2.926$ for 2D materials with covalent bonds by fitting fatigue experiments conducted on graphene (42, 36) (*SI Appendix*, Fig. S9*A*). The error in N_c, associated with uncertainties in K_{Ic}, can be calculated by differentiating **4** with respect to K_{Ic} (or J_c using the relationship $K_{Ic}^2 = EJ_c$). Such a calculation reveals that the error depends on both the value of J_c and the accuracy of its measurement. In *SI Appendix*, Fig. S9*B*, the minimum and maximum errors that could occur in the estimation of N_c as a result of the accuracy of the toughness measurement are plotted in log scale. The plot highlights that for different 2D materials, the relative error in estimating N_c can vary from ∼21 to ∼8,100% (these errors correspond to the toughness measurement errors reported in this study and in ref. 15, respectively) if the material is $MoSe_2/MoS_2$ (J_c ∼ 3.1 N/m) or from ∼5.6 to ∼2,100%, if the material is h-BN (J_c ∼ 11.5 N/m). Such overestimations in N_c, resulting from poor accuracy in the measurement of toughness, would adversely affect the reliability and adoption of nanodevices.

Conclusion

Using an integrated framework combining HRTEM experiments and a general potential-parameterizing approach, which can optimally capture bond dissociation, we report the measurement and prediction of the intrinsic fracture properties of as-synthesized monolayer $MoSe_2$ and MoS_2, two examples of the 2H-TMDs family. The measurements of fracture energy achieved via strain and stress mapping in the vicinity of the crack tip and computation of the J-integral confirm the quasi-brittle nature of the two materials and the applicability of the Griffith criterion (with nonlinearity in a process zone of approximately 1 nm in length). Quantitative agreement between HRTEM experiments and MD simulations is achieved through parameterization of the Tersoff interatomic potential, accounting for the accurate description of large-deformation pathways. As such, the framework opens opportunities for experimental validation of computational approaches used in the design of materials in the spirit of the materials genome initiative. Indeed, we anticipate that the approach herein reported will serve as a general method for probing mechanical properties and fracture energy of other 2D materials, especially emergent ones with applications to energy (battery electrodes, catalysts, low-friction materials), health (biosensors, cellular scaffolds), and next-generation electronics (flexible electronics, transistors, nanoelectromechanical systems). Likewise, we anticipate the extension of the combined experimental–computational methodology to applications involving thermomechanical and dynamic loading.

Data, Materials, and Software Availability. All study data are included in the article and/or supporting information.

ACKNOWLEDGMENTS. This work was funded by NSF Grant CMMI 1953806 and Office of Naval Research Grant N00014-22-1-2133. Work performed at the Center for Nanoscale Materials, a U.S. Department of Energy Office of Science User Facility, was supported by the U.S. DOE, Office of Basic Energy Sciences, under Contract No. DE-AC02-06CH11357.

Author affiliations: [a]Theoretical and Applied Mechanics Program, Northwestern University, Evanston, IL 60208; [b]Department of Materials Science and NanoEngineering, Rice University, Houston, TX 77005; [c]Center for Nanoscale Materials, Argonne National Laboratory, Lemont, IL 60439; and [d]Department of Mechanical Engineering, Northwestern University; Evanston, IL 60208

Author contributions: Xu Zhang, H.N., and H.D.E. designed research; Xu Zhang and H.N. performed research; J.W. contributed new reagents/analytic tools; Xu Zhang, H.N., J.W., and H.D.E. analyzed data; Xiang Zhang and P.M.A. synthesized the materials; and Xu Zhang, H.N., Xiang Zhang, P.M.A., J.W., and H.D.E. wrote the paper.

1. D. Akinwande *et al.*, Graphene and two-dimensional materials for silicon technology. *Nature* **573**, 507–518 (2019).
2. X. Zhang, L. Hou, A. Ciesielski, P. Samorì, 2D materials beyond graphene for high-performance energy storage applications. *Adv. Energy Mater.* **6**, 1600671 (2016).
3. Y. D. Kim *et al.*, Bright visible light emission from graphene. *Nat. Nanotechnol.* **10**, 676–681 (2015).
4. D. Jariwala, V. K. Sangwan, L. J. Lauhon, T. J. Marks, M. C. Hersam, Emerging device applications for semiconducting two-dimensional transition metal dichalcogenides. *ACS Nano* **8**, 1102–1120 (2014).
5. C. W. Lee, J. M. Suh, H. W. Jang, Chemical sensors based on two-dimensional (2D) materials for selective detection of ions and molecules in liquid. *Front Chem.* **7**, 708 (2019).
6. D. Akinwande *et al.*, A review on mechanics and mechanical properties of 2D materials: Graphene and beyond. *Extreme Mech. Lett.* **13**, 42–77 (2017).
7. L. Huang *et al.*, In situ scanning transmission electron microscopy observations of fracture at the atomic scale. *Phys. Rev. Lett.* **125**, 246102 (2020).
8. S. Wang *et al.*, Atomically sharp crack tips in monolayer MoS_2 and their enhanced toughness by vacancy defects. *ACS Nano* **10**, 9831–9839 (2016).
9. R. A. Bernal *et al.*, Intrinsic Bauschinger effect and recoverable plasticity in pentatwinned silver nanowires tested in tension. *Nano Lett.* **15**, 139–146 (2015).
10. B. Peng *et al.*, Measurements of near-ultimate strength for multiwalled carbon nanotubes and irradiation-induced crosslinking improvements. *Nat. Nanotechnol.* **3**, 626–631 (2008).
11. R. Ramachandramoorthy, R. Bernal, H. D. Espinosa, Pushing the envelope of in situ transmission electron microscopy. *ACS Nano* **9**, 4675–4685 (2015).
12. R. Ramachandramoorthy, W. Gao, R. Bernal, H. Espinosa, High strain rate tensile testing of silver nanowires: Rate-dependent brittle-to-ductile transition. *Nano Lett.* **16**, 255–263 (2016).

13. Y. Zhu, H. D. Espinosa, An electromechanical material testing system for in situ electron microscopy and applications. *Proc. Natl. Acad. Sci. U.S.A.* **102**, 14503–14508 (2005).
14. P. Zhang *et al.*, Fracture toughness of graphene. *Nat. Commun.* **5**, 3782 (2014).
15. Y. Yang *et al.*, Intrinsic toughening and stable crack propagation in hexagonal boron nitride. *Nature* **594**, 57–61 (2021).
16. X. Zhang *et al.*, Multi-objective parametrization of interatomic potentials for large deformation pathways and fracture of two-dimensional materials. *npj Comput. Mater.* **7**, 113 (2021).
17. F. Z. Li, C. F. Shih, A. Needleman, A comparison of methods for calculating energy release rates. *Eng. Fract. Mech.* **21**, 405–421 (1985).
18. J. R. Rice, A path independent integral and the approximate analysis of strain concentration by notches and cracks. *J. Appl. Mech.* **35**, 379–386 (1968).
19. S. Dong *et al.*, Facile fabrication of 2D material multilayers and vdW heterostructures with multimodal microscopy and AFM characterization. *Mater. Today* **52**, 31–42 (2022).
20. T. H. Ly, J. Zhao, M. O. Cichocka, L.-J. Li, Y. H. Lee, Dynamical observations on the crack tip zone and stress corrosion of two-dimensional MoS2. *Nat. Commun.* **8**, (2017).
21. Y. Manzanares-Negro *et al.*, Confined Crack Propagation in MoS 2 Monolayers by Creating Atomic Vacancies. *ACS Nano* **15**, 1210–1216 (2021).
22. H.-P. Komsa *et al.*, Two-dimensional transition metal dichalcogenides under electron irradiation: Defect production and doping. *Phys. Rev. Lett.* **109**, 035503 (2012).
23. H.-P. Komsa, S. Kurasch, O. Lehtinen, U. Kaiser, A. V. Krasheninnikov, From point to extended defects in two-dimensional MoS${}_{2}$: Evolution of atomic structure under electron irradiation. *Phys. Rev. B* **88**, 035301 (2013).
24. X. Zhang, X. Zhang, P. M. Ajayan, J. Wen, H. D. Espinosa (Edge-mediated annihilation of vacancy clusters in monolayer molybdenum diselenide (MoSe2) under electron beam irradiation. *Small* **18**, 2105194 (2022).
25. T. K. Patra *et al.*, Defect dynamics in 2-D MoS_2 probed by using machine learning, atomistic simulations, and high-resolution microscopy. *ACS Nano* **12**, 8006–8016 (2018).
26. J. Tersoff, New empirical approach for the structure and energy of covalent systems. *Phys. Rev. B Condens. Matter* **37**, 6991–7000 (1988).
27. J. Hutchinson, Singular behaviour at the end of a tensile crack in a hardening material. *J. Mech. Phys. Solids* **16**, 13–31 (1968).
28. J. Madsen, P. Liu, J. B. Wagner, T. W. Hansen, J. Schiøtz, Accuracy of surface strain measurements from transmission electron microscopy images of nanoparticles. *Adv. Struct. Chem. Imaging* **3**, 14 (2017).
29. R. E. Jones, J. A. Zimmerman, The construction and application of an atomistic J-integral via Hardy estimates of continuum fields. *J. Mech. Phys. Solids* **58**, 1318–1337 (2010).
30. A. P. Thompson *et al.*, LAMMPS: A flexible simulation tool for particle-based materials modeling at the atomic, meso, and continuum scales. *Comput. Phys. Commun.* **271**, 108171 (2022).
31. N. C. Admal, E. B. Tadmor, A unified interpretation of stress in molecular systems. *J. Elast.* **100**, 63–143 (2010).
32. V. A. Kuzkin, Comment on the calculation of forces for multibody interatomic potentials. arXiv [Preprint] (2010). https://arxiv.org/abs/1003.5267 (Accessed 27 March 2010).
33. J. Lin, S. T. Pantelides, W. Zhou, Vacancy-induced formation and growth of inversion domains in transition-metal dichalcogenide monolayer. *ACS Nano* **9**, 5189–5197 (2015).
34. M. S. Elapolu, A. Tabarraei, X. Wang, D. E. Spearot, Fracture mechanics of multi-layer molybdenum disulfide. *Eng. Fract. Mech.* **212**, 1–12 (2019).
35. R. A. Soler-Crespo *et al.*, Atomically thin polymer layer enhances toughness of graphene oxide monolayers. *Matter* **1**, 369–388 (2019).
36. X. Zhang, H. Nguyen, M. Daly, S. T. Nguyen, H. D. Espinosa, Nanoscale toughening of ultrathin graphene oxide-polymer composites: Mechanochemical insights into hydrogen-bonding/van der Waals interactions, polymer chain alignment, and steric parameters. *Nanoscale* **11**, 12305–12316 (2019).
37. S. Zhang, J. Zhang, Fatigue and its effect on the mechanical and thermal transport properties of polycrystalline graphene. *J. Mater. Sci.* **56**, 10367–10381 (2021).
38. X. Wei *et al.*, Plasticity and ductility in graphene oxide through a mechanochemically induced damage tolerance mechanism. *Nat. Commun.* **6**, 8029 (2015).
39. A. Castellanos-Gomez *et al.*, Deterministic transfer of two-dimensional materials by all-dry viscoelastic stamping. *2D Materials* **1**, 011002 (2014).
40. A. Gurarslan *et al.*, Surface-energy-assisted perfect transfer of centimeter-scale monolayer and few-layer MoS_2 films onto arbitrary substrates. *ACS Nano* **8**, 11522–11528 (2014).
41. M. Graf *et al.*, Fabrication and practical applications of molybdenum disulfide nanopores. *Nat. Protoc.* **14**, 1130–1168 (2019).
42. T. Cui *et al.*, Fatigue of graphene. *Nat. Mater.* **19**, 405–411 (2020).
43. T. Jin, J. Kang, E. Su Kim, S. Lee, C. Lee, Suspended single-layer MoS2 devices. *J. Appl. Phys.* **114**, 164509 (2013).
44. A. Castellanos-Gomez *et al.*, Single-layer MoS(2) mechanical resonators. *Adv. Mater.* **25**, 6719–6723 (2013).
45. S. S. P. Nathamgari *et al.*, Nonlinear mode coupling and one-to-one internal resonances in a monolayer WS2 nanoresonator. *Nano Lett.* **19**, 4052–4059 (2019).
46. A. K. Majee, Z. Hemmat, C. J. Foss, A. Salehi-Khojin, Z. Aksamija, Current rerouting improves heat removal in few-layer WSe**2** devices. *ACS Appl. Mater. Interfaces* **12**, 14323–14330 (2020).
47. R. Zhang, V. Koutsos, R. Cheung, Elastic properties of suspended multilayer WSe2. *Appl. Phys. Lett.* **108**, 042104 (2016).
48. S. Mathew *et al.*, Temperature dependent structural evolution of WSe2: A synchrotron X-ray diffraction study. *Condens. Matter* **5**, 76 (2020).